Resolving rotationally excited states of ultralong-range Rydberg molecules

Y. Lu,[1] J. D. Whalen,[1] S. K. Kanungo,[1] T. C. Killian,[1] F. B. Dunning,[1] S. Yoshida,[2] and J. Burgdörfer[2]
[1]*Department of Physics and Astronomy, Rice University, Houston, Texas 77005-1892, USA*
[2]*Institute for Theoretical Physics, Vienna University of Technology, Vienna A-1040, Austria, EU*

(Received 17 March 2022; revised 30 June 2022; accepted 21 July 2022; published 16 August 2022)

We report experimental observations of the rotational structure in photoassociative spectroscopy of ultralong-range Rydberg molecules (ULRRMs) in an ultracold gas of ^{86}Sr. ULRRM spectroscopy probes scattering wave functions at much larger internuclear separations than photoassociative spectroscopy of low-lying electronic states. At such separations photon recoil momentum can lead to the transfer of significant angular momentum to the Rydberg molecule, evidence of which is provided through the distribution of excited rotational states. The visibility of the rotational structure is enhanced because, for collisions between ground-state ^{86}Sr atoms, the large, near-resonant s-wave scattering length approaches the size of the ULRRM. Similar enhancement is not seen for ^{84}Sr, which has a much smaller scattering length. Results are interpreted with the aid of a theory that accounts for the recoil momentum associated with photoexcitation and the large *s*-wave scattering length in the entrance channel. While the observed rotational splittings and the qualitative trends in the relative intensities of the spectral features are well described by theory, the effects of recoil momentum are more prominent in the measured data than in the theory.

DOI: 10.1103/PhysRevA.106.022809

I. INTRODUCTION

Ultralong-range Rydberg molecules (ULRRMs), which comprise a Rydberg atom in whose electron cloud are embedded one or more very weakly bound ground-state atoms, have been the focus of much recent interest because of their novel physical and chemical properties [1–17]. These have been exploited, for example, to create so-called trilobite molecules which, despite being homonuclear, possess large permanent electric dipole moments. When the Rydberg electron orbit encloses tens to hundreds of ground-state atoms, many-body effects such as the creation of Rydberg polarons [15–18] can be studied. Whereas the vibrational structure of Rydberg dimer molecules has been examined in some detail [2,17,19], their rotational structure remains largely unexplored. Rotational spectroscopy is extremely powerful for probing molecular structure and *in situ* isotopologue-specific detection [20]. In ULRRM it reveals a rich collection of novel phenomena.

In the present work $^3S_1$ Rydberg dimers with $29 < n < 39$ are produced by photoexcitation in an ultracold Sr gas. In the ultracold regime, atom-atom scattering with partial waves higher than *s* wave is strongly suppressed for ^{86}Sr, but higher angular momentum channels can still play a prominent role in ULRRM creation because of the large molecular size [21]. As is the case in traditional photoassociative spectroscopy of low-lying electronic states [22], interactions between ground-state atoms in the ultracold gas can have a strong influence on the excitation spectrum when the *s*-wave scattering length a_s is comparable to the size of the molecule (for ^{86}Sr $a_s = 811a_0$ [23]). Such near-resonant scattering processes are critical to the results presented here and are key to the increase in visibility of rotational excitation. Similar considerations do not apply for ^{84}Sr, which has a much smaller scattering length. For ^{86}Sr the interplay of quantum statistics and the selection rules for rotational transitions leads to clear signatures in the rotational structure of non-Franck-Condon transitions, which arise because of photon recoil and the large size of the Rydberg molecule.

Rotational structure has been observed using Rb($25p$) butterfly Rydberg molecules [24]. This special class of Rydberg molecules is associated with the presence of a low-energy *p*-wave shape resonance in electron-rubidium scattering which results in increased binding energies. This work focused on the orientation of the molecules with an electric field and the resulting "pendular" states. Rotational structure was not examined in detail. ^{86}Sr provides several advantages for studying rotational excitation. The absence of a *p*-wave electron scattering resonance and the excitation to an *ns* Rydberg orbital removes complications associated with the electronic orbital angular momentum degree of freedom from the analysis of the rotational structure of the molecular system. The rotational structure of ULRRMs was considered theoretically in Ref. [25]. In the current work this theoretical model is extended to include incoming partial waves other than the *s* wave, the photon momentum recoil, and ground-state atom interactions. Moreover, we find that thermal averaging is a key to reproducing the excitation spectra measured in the current experiments.

The binding of Rydberg molecules results from scattering of the Rydberg electron by a ground-state atom. The resulting molecular potential, calculated using a two-active-electron model and a Fermi pseudopotential to describe the electron–ground-state-atom interaction, is shown in Fig. 1 for $n = 29$.

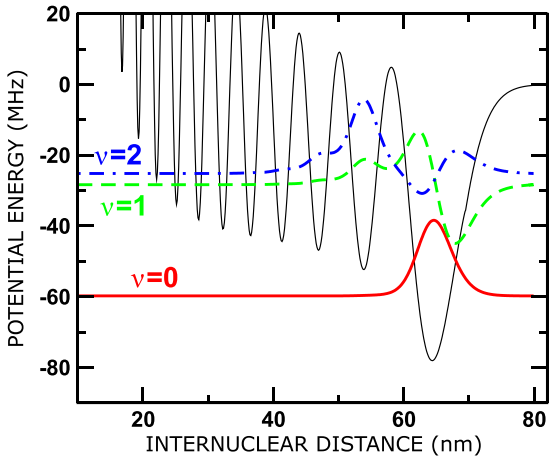

FIG. 1. Calculated molecular potential for a $5s29s\ ^3S_1 - 5s^2\ ^1S_0$ strontium atom pair. The calculated vibrational wave functions, multiplied by the radial coordinate R, for the $\nu = 0$, 1, and 2 vibrational states are also included, and the horizontal axis for each shows its binding energy.

The potentials for the other values of n studied here display similar characteristics, each mirroring the electron probability density distribution in the parent Rydberg atom. Figure 1 also includes the calculated wave functions for the $\nu = 0$, 1, and 2 vibrational levels. Of particular interest here is the $\nu = 0$ wave function, which is strongly localized in the outermost well of the molecular potential at an internuclear separation $R_n \sim 1.8(n-\delta)^2 a_0$, where a_0 is the Bohr radius and δ is the quantum defect, ~3.37 for $^3S_1$ states. For $n = 29$ this gives $R_n \sim 1200a_0$. This localization permits, through the choice of n, remarkable control over the molecular bond length and has been exploited to measure pair-correlation functions $g^{(2)}(R)$ in low-temperature quantum gases of identical bosons (^{84}Sr) and identical fermions (spin-polarized ^{87}Sr) to examine the effects of quantum statistics [26]. Spin-orbit coupling vanishes for Rydberg molecules involving strontium $^3S_1$ states. For this situation Hund's case B applies, and the molecular levels are characterized by the rotational quantum number N, which, in the present case, corresponds to the orbital angular momentum of the molecule. The observed distribution of rotationally excited states, in particular the observation of states with an odd number of rotational quanta, indicates the breakdown of the Franck-Condon principle induced by the recoil momentum associated with the photons that photoexcite the Rydberg electron. Understanding the rotational structure of long-range Rydberg molecules will further their use as a probe of quantum gases and is important for proposals to use high-n Rydberg molecules to create low-energy ions in a quantum gas and study their behavior [27].

II. EXPERIMENTAL APPROACH

The present experimental techniques are described in detail elsewhere [28,29]. Briefly, strontium atoms are laser cooled to ~2 μK and loaded into a "pancake"-shaped optical dipole trap (ODT) formed using two crossed focused planar 1.064-μm laser beams. Evaporative cooling is used to further lower the atom temperature. (All measurements of Rydberg molecule formation are undertaken with the magnetic fields used in the initial atom trapping reduced to near zero, $\lesssim$70 mG.) Rydberg atoms or molecules are created through two-photon excitation via the $5s5p\ ^3P_1$ intermediate state. The first photon at 689 nm has a fixed blue detuning of 15 MHz from the $^3P_1$ level; the second photon at 320 nm completes the transition to the selected $5sns\ ^3S_1$ Rydberg level. Both ^{84}Sr and ^{86}Sr used in this experiment have a nuclear spin of zero and thus no hyperfine structure. Both lasers are stabilized to a high-finesse, ultralow-expansion optical cavity. To either minimize or maximize the net momentum transfer, i.e., the photon recoil, that results from photoexcitation, the excitation lasers either counterpropagate or copropagate, respectively. In both cases, the polarizations of the two excitation lasers are linear and parallel to each other. Most of the present data were recorded using counterpropagating laser beams to minimize the photon recoil. The photoexcitation lasers are applied for 10 μs, after which the Rydberg atoms or molecules produced are detected by ionizing them in a pulsed electric field. The resulting electrons are directed to a microchannel plate for detection and counted. Experimental limitations on the size of the ionizing field that could be generated in the experimental region restricted measurements to states with values of $n >$ 28. Excitation rates are kept low ($\lesssim$1 per laser pulse) to avoid any Rydberg-Rydberg interactions, and ~1000 experimental cycles can be performed using each cold-gas sample. For measurements with ^{86}Sr, where inelastic collisions can lead to rapid trap loss [30], the ODT (which has dimensions of $\sim 230 \times 130 \times 30\ \mu\text{m}^3$ with the tight axis along gravity) was loaded with ~1–2 $\times 10^5$ atoms, and the peak trap density was limited to $\sim 2 \times 10^{12}$ cm^{-3}. For comparative studies using ^{84}Sr, the ODT was loaded with ~5–10 $\times 10^5$ atoms, resulting in peak trap densities of up to $\sim 1 \times 10^{13}$ cm^{-3}. The final atom number and temperature were determined through absorption imaging on the $5s^2\ ^1S_0 \rightarrow 5s5p\ ^1P_1$ transition following the release of the atoms from the trap and a fall time of ~15 ms.

III. RESULTS

A. Observations

Figure 2 shows excitation spectra recorded when creating ^{86}Sr dimers in the ground $\nu = 0$ vibrational state using counterpropagating laser beams for selected values of n in the range $29 \leqslant n \leqslant 39$ and a sample temperature of ~1.2 μK. Each data set was recorded using similar trap conditions and is scaled to compensate for variations in density and laser powers. The uncertainties inherent in this scaling, however, are relatively large and are estimated to amount to $\sim \pm$ 20%–30%. Each data set is also scaled by $(n-\delta)^{-3.5}$. This compensates for both the $1/(n-\delta)^3$ dependence in the electronic dipole transition matrix element and the dependence of the Franck-Condon (FC) overlap factor on the Rydberg orbital size which, according to direct numerical integration, introduces an additional $(n-\delta)^{6.5}$ scaling. The scaling of the FC factor can be understood from the following argument. The ground vibrational wave function is localized at $R_n \sim (n-\delta)^2$ with a width σ scaling as $\sim(n-\delta)^2$ [13]. The overlap integral with a uniform initial atom distribution thus scales as $(n-\delta)^3$ [31], and the squared Franck-Condon factor

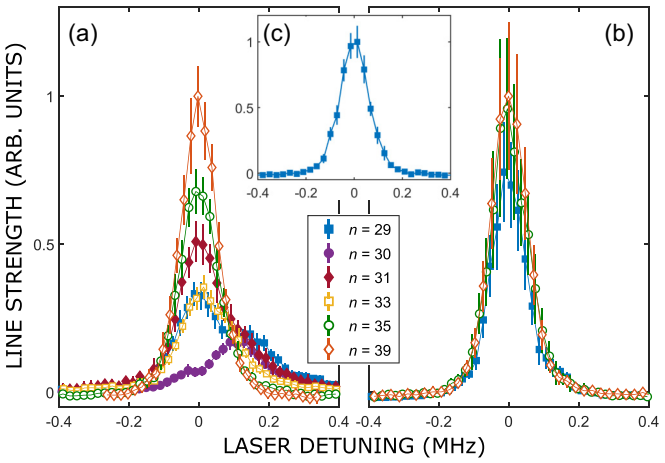

FIG. 2. Excitation spectra for the creation of $\nu = 0$ dimers in (a) a 1.2 μK ^{86}Sr gas and (b) a 1.2 μK ^{84}Sr gas for the values of n indicated when using counterpropagating excitation beams. In each data set the dimer production rates are scaled to equal trap densities and laser powers, and the error bars include the systematic error associated with this scaling. The measurements are also scaled by $(n-\delta)^{-3.5}$ (see text). To highlight changes in line shape the data sets in (a) and (b) are scaled to the same maximum peak heights. Zero detuning in each spectrum is taken to be the fitted center (see Fig. 3) of the $N = 0$ state for low n ($n = 29 - 33$) and the peak position for high n ($n = 35, 39$). For reference, the $n = 29$ atomic Rydberg excitation line is shown in (c).

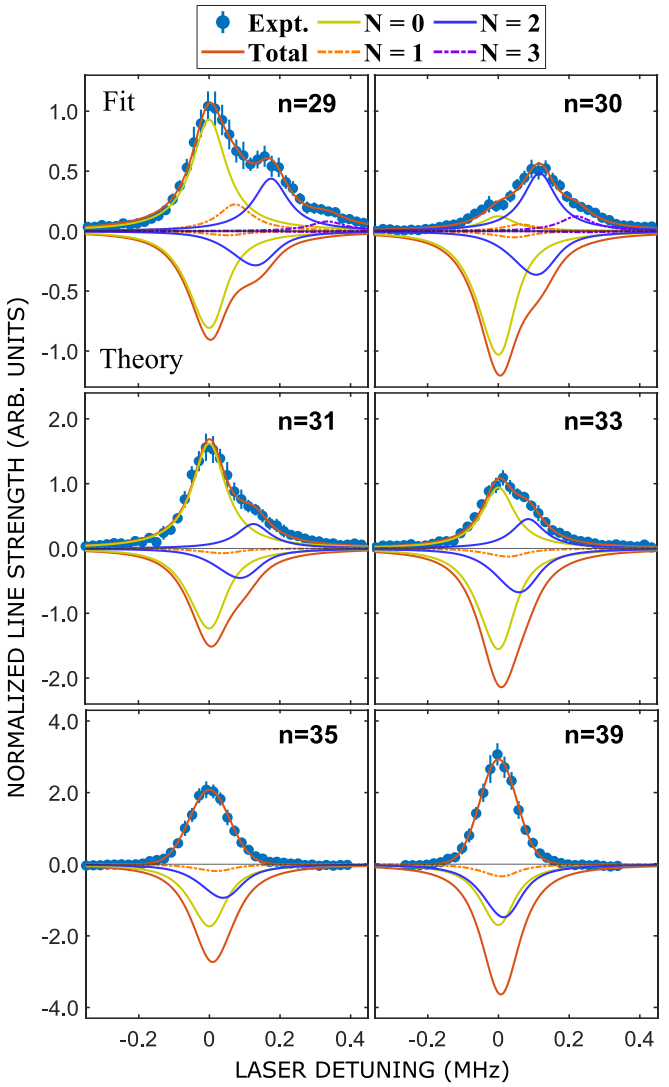

FIG. 3. Measured (Expt.), fit (Fit), and calculated (Theory) line profiles for the creation of $\nu = 0$ dimers in a 1.2 μK ^{86}Sr gas and the values of n indicated. The experimental results include an $(n-\delta)^{-3.5}$ scaling (see text). The calculated profiles for all n are scaled by a single factor, so that the integrated area agrees with experimental measurement at $n = 31$. The measured profiles for $n = 29$ and 30 (31 and 33) are fit with the sum of four (two) Lorentzians assigned to the rotational states indicated in the legend with widths constrained to that of the corresponding atomic Rydberg state (see text). A single Lorentzian fit is shown for $n \geqslant 35$. The contributions to the (mirrored) theoretical predictions from different rotational states are also shown. Zero detuning in each experimental spectrum is taken to be the fitted center of the $N = 0$ state for low n ($n = 29 - 33$) and the peak position for high n ($n = 35, 39$). The error bars show the statistical uncertainty in the measurements. Note that the scales of the vertical axes change from the top to the bottom.

scales as $(n-\delta)^6$, close to the numerical result which includes more accurate scaling of R_n and σ calculated from the molecular potential. Experimental and numerical studies for similar values of n using a cold unpolarized ^{87}Sr gas for which the pair-correlation function is constant, i.e., $g^{(2)}(R) = 1$, and atom-atom interactions are negligible confirmed the overall $(n-\delta)^{3.5}$ scaling of the dimer signal strength [26]. However, as seen in Fig. 2, even after accounting for this n scaling, a marked n dependence remains in the dimer production rate for the strongly interacting isotope ^{86}Sr. Representative results obtained when creating $\nu = 0$ ^{84}Sr dimers and an atomic Rydberg state are included in Fig. 2 for comparison.

Symmetric ^{84}Sr dimer excitation profiles were observed for all values of n, with widths that were similar to those seen when exciting the corresponding atomic Rydberg state. This width results primarily from the linewidth of the 320-nm radiation, which is generated by doubling the 640-nm output of an optical-parametric-oscillator system, together with a small contribution from the finite lifetime of the excited state (~19 kHz at $n = 30$). The effective overall linewidth was typically in the range of 120 to 140 kHz. To monitor its variation, for each value of n, measurements of the atomic linewidth were undertaken prior to measurement of the corresponding dimer line shapes. Whereas the line profiles for the production of ^{84}Sr dimers are essentially independent of n (see Fig. 2), those for ^{86}Sr dimer formation display a marked n dependence. At the lower values of n the line profiles broaden and develop pronounced "shoulders."

Consider initially the excitation profile for $n = 29$, which is shown, together with those for other values of n, in Fig. 3. The profile contains significant structure. Attempts were made to fit the profile using the sum of two Lorentzians with linewidths constrained to that of the atomic line which would correspond to the creation of just two different final states. Such fits, however, failed to reproduce well the observed features. The fitting procedure was therefore extended to include four Lorentzians whose heights and locations (but not widths) were

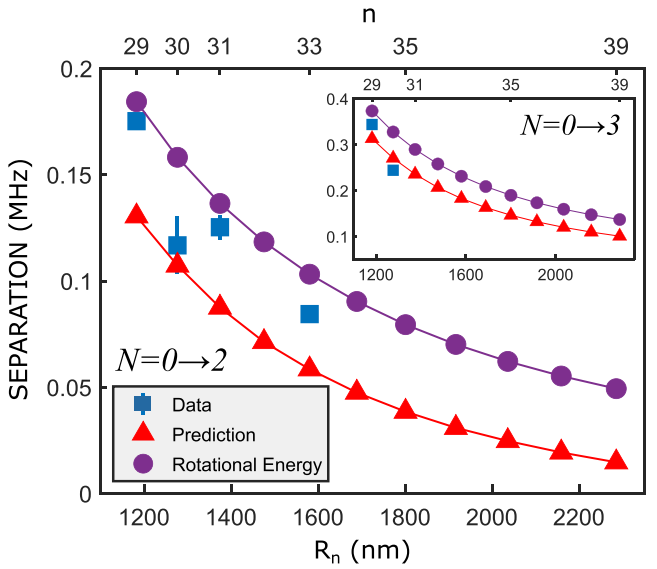

FIG. 4. n-dependence of the rotational energy spacings $E_{v,N=2} - E_{v,N=0}$ expressed as a function of internuclear separation R_n. •, evaluated from the centrifugal energy [Eq. (1)]; ■, separation of the positions of the corresponding Lorentzians used to fit the experimental data; and ▲, extracted from the calculated excitation spectra (see text). The inset shows the separation of the $N = 0$ and 3 levels. The calculated and measured values are for a sample temperature of ∼1.2 μK.

treated as fit variables. With this increase in fit parameters, it was possible to obtain excellent fits to the experimental results. This is demonstrated in Fig. 3, which also shows the individual contributions from each of the four component Lorentzians to the overall fit profile. To identify the source of these components we consider the dimer rotational structure.

Assuming the molecules behave as a rigid rotor, their rotational energy levels can be approximated by

$$E_{v,N} = E_{v,N=0} + \frac{\hbar^2 N(N+1)}{2\mu R_n^2}, \tag{1}$$

where N is the rotational quantum number, μ is the reduced mass, and R_n is the ULRRM internuclear separation, $R_n \sim 1.8(n-\delta)^2 a_0$.

As shown in Fig. 4, for $n = 29$ Eq. (1) predicts a separation between the $N = 0$ and $N = 2$ rotational levels, $E_{v,N=2} - E_{v,N=0}$, of 180 kHz, which is close to the separation between the two largest features present in the fit shown in Fig. 3. Furthermore, as shown in the inset in Fig. 4, the separation between the two extreme features in the fit, ∼335 kHz, is in reasonable agreement with that between the $N = 0$ and $N = 3$ levels suggested by Eq. (1). Finally, the separation between the first and second features in the fit, ∼70 kHz, is somewhat larger than that predicted between the $N = 0$ and $N = 1$ levels, ∼40 kHz. However, these two features cannot be reliably discriminated given the present instrumental linewidth precluding other than qualitative estimates of their relative heights and positions. Nonetheless, it appears reasonable to assign the observed structure in the line profile to the creation of dimer molecules in rotationally excited states, the majority of these being in the $N = 2$ state but including significant contributions from the $N = 1$ and $N = 3$ states. As is evident from Fig. 3, the line profile for $n = 30$ can also be well fit by the sum of four Lorentzians whose relative sizes and positions are also shown. Again, the separations between the various features are consistent with the production of dimers in rotationally excited states.

For $n = 31$ and 33 the experimental linewidth is too large to allow resolution of the $N = 0$ and 1 rotational levels, and no significant contribution from $N = 3$ levels is apparent. The data for $n = 31$ and 33 are therefore fit using the sum of just two Lorentzians. As shown in Fig. 4, the separation between these two components is consistent with the separation between the $N = 0$ and 2 states predicted by Eq. (1), suggesting that these states provide the major contributions to the dimer spectrum. For values of $n \geqslant 35$ no structure can be resolved, and a single Lorentzian provides a good fit to the data. Inspection of Fig. 3 shows that the relative contributions to overall dimer production for $n = 30$ are rather different than those seen for $n = 29$. In particular, the integrated ground-state dimer signal for $n = 30$ is much smaller than that for $n = 29$ (and $n = 31$), indicating that the production of dimers in the ground rotational state is suppressed. Interestingly, no similar large reduction is observed in the production of $N = 2$ and 3 rotationally excited dimers.

To support the rotational level assignments and to quantitatively analyze the data, we present a theoretical description of the photoexcitation process.

B. Theoretical analysis

The structure apparent in the photoexcitation spectra for ^{86}Sr dimers can be understood by extending the theory developed in earlier studies of dimer formation to include the effects of ground-state atom interactions in the entrance channel and recoil momentum associated with photoexcitation. We first consider the interaction of a pair of atoms with a laser field. Each atom consists of an electron and the ion core. The positions of the ions are denoted by $\vec{R}_A$ and $\vec{R}_B$. Taking into account that the mass of the strontium ion M_I is very large compared to the electron mass ($M_I = 1.57 \times 10^5$ a.u.), $\vec{R}_A$ and $\vec{R}_B$ coincide with the center of mass of each atom. This should be distinguished from the center of mass for the pair of atoms given by $\vec{R}_{\rm CM} = (\vec{R}_A + \vec{R}_B)/2$. The positions of the valence electrons that can be excited to a Rydberg state are denoted by $\vec{r}_A$ or $\vec{r}_B$ with respect to the ion core to which each is bound.

A Rydberg dimer is formed by a weak perturbation to isolated atoms. Therefore, the two atoms in the molecule may be treated as composite, identical, bosonic particles, just as they are in the initial state of the colliding free atoms. In the above-defined coordinate system, the Hamiltonian of two interacting atoms is invariant with an exchange of both electron and ion coordinates simultaneously, and correspondingly, the wave functions are symmetric with respect to this overall exchange. This is different from a typical description of molecules in which the symmetry of wave functions is defined with an exchange of only electron coordinates (or ion coordinates).

The laser-atom interaction for laser field α can be written as

$$\sum_{i=A,B} V_\alpha(\vec{R}_i, \vec{r}_i) = \sum_{i=A,B} [e(\vec{R}_i + \vec{r}_i) \cdot \hat{e}_\alpha F_\alpha e^{i\vec{\kappa}_\alpha \cdot (\vec{R}_i + \vec{r}_i) - i\omega_\alpha t} - e\vec{R}_i \cdot \hat{e}_\alpha F_\alpha e^{i\vec{\kappa}_\alpha \cdot \vec{R}_i - i\omega_\alpha t}] \quad (2)$$

and is given in the dipole approximation, using $e^{i\vec{\kappa}_\alpha \cdot \vec{r}_i} \simeq 1$, by

$$\sum_{i=A,B} V_\alpha(\vec{R}_i, \vec{r}_i) \simeq \sum_{i=A,B} e\vec{r}_i \cdot \hat{e}_\alpha F_\alpha e^{i\vec{\kappa}_\alpha \cdot \vec{R}_i - i\omega_\alpha t}, \quad (3)$$

where $\hat{e}_\alpha$ is the polarization unit vector, F_α is the amplitude, and $\vec{\kappa}_\alpha$ is the wave vector of the laser field with frequency (or energy in atomic units) ω_α. The position-dependent phase $e^{i\vec{\kappa}_\alpha \cdot \vec{R}_i}$, or "boost" factor, describes the transfer of the linear momentum of the absorbed photons to the ion core, or, equivalently, to the atom. When a Rydberg dimer is formed through two-photon excitation with laser fields α and β, the recoil momentum is shared between the center-of-mass translational motion of the pair and the relative motion between the two constituents of the pair according to the factor

$$\begin{aligned} e^{i\vec{\kappa} \cdot \vec{R}_A} &= e^{i\vec{\kappa} \cdot \vec{R}_{\rm CM}} e^{-i(\vec{\kappa}/2) \cdot \vec{R}}, \\ e^{i\vec{\kappa} \cdot \vec{R}_B} &= e^{i\vec{\kappa} \cdot \vec{R}_{\rm CM}} e^{i(\vec{\kappa}/2) \cdot \vec{R}}, \end{aligned} \quad (4)$$

where $\vec{\kappa} = \vec{\kappa}_\alpha + \vec{\kappa}_\beta$ and $\vec{R} = \vec{R}_B - \vec{R}_A$ denotes the relative position of the ions.

Considering the absorption of photons by the atom pair as a scattering process, the initial scattering state is denoted by

$$|\chi_i\rangle = |\vec{k}'_{\rm CM}; k, N', M'_N; g, g\rangle, \quad (5)$$

where $\hbar\vec{k}'_{\rm CM}$ is the linear momentum of the center-of-mass motion and the electronic state $|g\rangle$ represents the ground state, $5s^2\ {}^1S_0$. We choose a partial-wave representation $|k, N', M'_N\rangle$ for the relative motion, and $\hbar\vec{k}$ is the relative momentum. Due to the exchange symmetry of bosons applicable to both ^{84}Sr and ^{86}Sr pairs, only even rotational quantum numbers $N' = 0, 2, 4, \ldots$ are allowed. The corresponding final scattering state after two-photon absorption can be written as

$$|\chi_f\rangle = \frac{1}{\sqrt{2}}[|\vec{k}_{CM}; \nu, N, M_N; n, g\rangle + (-1)^N |\vec{k}_{CM}; \nu, N, M_N; g, n\rangle], \quad (6)$$

where $|n\rangle$ represents a Rydberg state. The very weak interaction between the Rydberg electron and the nearby ground-state atom allows the electronic excitation to be treated in lowest-order perturbation theory. The translational motion of the molecule is boosted by the recoil momentum, and $\hbar\vec{k}_{CM} = \hbar\vec{k}'_{\rm CM} + \hbar\vec{\kappa}$. In addition to the excitation of a vibrational state ν, the rotational quantum numbers can, in principle, also change. Since the total orbital angular momentum of the valence electrons of strontium vanishes, the rotational excitation can be represented by the two quantum numbers N and M_N which completely characterize the total mechanical angular momentum. Accordingly, the electronic state is assumed to be an unperturbed atom, i.e., Rydberg state $|rs\rangle = |5sns\ {}^3S_1\rangle$. The transition amplitude for the molecular degrees of freedom in the scattering process is proportional to the inelastic form factor

$$F_{\nu,N,M_N}(k, N', M'_N) = \frac{1}{\sqrt{2}} \langle \nu, N, M_N | [e^{-i(\vec{\kappa}/2) \cdot \vec{R}} + (-1)^N e^{i(\vec{\kappa}/2) \cdot \vec{R}}] | k, N', M'_N \rangle, \quad (7)$$

which resembles a FC overlap factor typically used for molecular spectroscopy. Compared to a typical FC factor, it additionally includes the effects of photon recoil momentum, which leads to the excitation of not only vibrational but also rotational states.

To evaluate the form factor explicitly, we use the spherical representations of both the initial asymptotic scattering state of the atomic pair,

$$\langle \vec{R} | k, N', M'_N \rangle = \tilde{j}_{N'}(kR) Y_{N'}^{M'_N}(\hat{R}), \quad (8)$$

and the final state of the Rydberg molecule,

$$\langle \vec{R} | \nu, N, M_N \rangle = \mathcal{R}_{\nu,N}(R) Y_N^{M_N}(\hat{R}), \quad (9)$$

where $\mathcal{R}_{\nu,N}(R)$ is the radial wave function representing the vibrational motion. For Rydberg S states the third Euler angle becomes cyclic, and the Wigner rotation matrix reduces to a spherical harmonic $Y_N^{M_N}(\hat{R})$ describing the rotational excitation [25]. Only even $N' = 0, 2, \ldots$ contribute to the initial state [Eq. (8)]. Its phase-shifted spherical waves can be approximated by

$$\tilde{j}_{N'}(kR) = \begin{cases} \dfrac{\sin[k(R - a_s)]}{kR} & N' = 0, \\ j_{N'}(kR) & N' > 0, \end{cases} \quad (10)$$

where a_s is the s-wave scattering length and $j_{N'}(kR)$ is the spherical Bessel function. In Eq. (10) we have used the fact that the short-range interaction between the pair of ultracold ground-state Sr atoms significantly influences only the s-wave scattering. Using a partial-wave expansion of the boost factors $e^{\pm i(\vec{\kappa}/2) \cdot \vec{R}}$ which introduces the angular momentum λ and aligning $\vec{\kappa}$ along the z axis yield, for the form factor,

$$\begin{aligned} F_{\nu,N,M_N}(k, N', M'_N) &= (-1)^{M_N} \sqrt{2} \sqrt{(2N+1)(2N'+1)} \\ &\times \sum_{\lambda=|N-N'|}^{N+N'} (-i)^\lambda (2\lambda + 1) \begin{pmatrix} N & \lambda & N' \\ 0 & 0 & 0 \end{pmatrix} \\ &\times \begin{pmatrix} N & \lambda & N' \\ -M_N & 0 & M'_N \end{pmatrix} \\ &\times \int_0^\infty dR R^2 \mathcal{R}_{\nu,N}(R) j_\lambda(\kappa R/2) \tilde{j}_{N'}(kR). \end{aligned} \quad (11)$$

The selection rules for excitation of a molecular rotational state with quantum number N are $|N' - \lambda| \leqslant N \leqslant N' + \lambda$, with the additional requirement that $N + N' + \lambda$ must be an even integer. For a quantitative comparison with the experimental data we numerically evaluate the radial integral in Eq. (11) without further approximation. For qualitative

analysis and interpretation this radial integral can be approximated using the fact that the dimer vibrational wave function $\mathcal{R}_{v,N}(R)$ with $v = 0$ is strongly localized at $R = R_n$ (Fig. 1), allowing $R^2\mathcal{R}_{v,N}(R)$ in Eq. (11) to be replaced by $\delta(R - R_n)$. The contribution to the form factor from the term labeled by λ is then proportional to

$$F_{v,N,M_N}(k, N', M'_N) \propto j_\lambda(\kappa R_n/2)\tilde{j}_{N'}(kR_n). \tag{12}$$

The first factor governs the change in rotational quantum number $\lambda \simeq |\vec{N} - \vec{N}'|$ by the recoil photon momentum, and the second indicates the relative occupation amplitude of each partial wave N' of the initial scattering state.

Since in the current case the electronic excitation is nearly separable from the molecular degrees of freedom, the Hönl-London factor implies a conservation of rotational angular momentum during photoassociation [25]. Therefore, a change in rotational quantum number by a photon recoil represents an extension of the Franck-Condon principle, which states that electronically and vibrationally excited states are formed by "vertical" transitions at a given internuclear position. The nondiagonal transitions with $N - N' \neq 0$ observed here arise from the interplay of momentum recoil and the large molecular size. Since the electric dipole is localized on one atom when interacting with the lasers [Eq. (3)], the recoil momentum is transferred only to one atom, and this asymmetry leads to the transfer of angular momentum.

Averaging over a thermal Boltzmann distribution of relative momenta for atoms in the trap, the excitation strength $f(\omega)$ as a function of the laser frequency can be written as

$$f(\omega) \propto \left(\frac{\hbar^2}{2\pi\mu k_B T}\right)^{3/2} \sum_{N',M'_N} \int dk\, k^2 e^{-\hbar^2k^2/(2\mu k_B T)} \times \sum_{v,N,M_N} |F_{v,N,M_N}(k, N', M'_N)|^2 L_{v,N}(k, \omega), \tag{13}$$

where $L_{v,N}$ is a normalized line-shape function which, for the present experimental data, can be well approximated by a Lorentzian,

$$L_{v,N}(k, \omega) = \frac{1}{\pi}\left(\frac{2\Gamma}{4(\omega + \hbar k^2/(2\mu) - E_{v,N}/\hbar)^2 + \Gamma^2}\right), \tag{14}$$

with Γ being the FWHM of the instrumental linewidth. The peak position in Eq. (14) is determined by the initial relative kinetic energy of the collision pair, i.e., $E_{v,N} \simeq \hbar\omega + \hbar^2k^2/(2\mu)$, and energy conservation during excitation, where ω is the two-photon detuning from the unperturbed Rydberg atomic state. Due to the energy shift caused by the initial kinetic energy [Eq. (14)], the thermal averaging is expected to yield an asymmetric line profile extending towards the low-energy side which will be more pronounced at higher temperature [22].

C. Discussion

We consider first the limit of small photon recoil, which is realized to a good degree of approximation for counter-propagating laser beams. Here the momentum transfer is $\kappa/2 = (|\vec{\kappa}_\alpha| - |\vec{\kappa}_\beta|)/2 \sim 2.8 \times 10^{-4}$ a.u., and $\kappa R_n/2 \lesssim 0.4$ at $n = 30$. For $\kappa R_n/2 \ll 1$, $j_\lambda(\kappa R_n/2)$ tends to $\delta_{\lambda,0}$, i.e., $N = N'$. In this regime, the rotational angular momentum of the collision pair is expected to be preserved, and the selection rules, combined with the symmetry of the initial state, suggest that principally, molecular rotational states with even values of N will be created. This is illustrated in Fig. 3, which includes the calculated overall excitation profiles together with the contributions from different rotational states. As seen in Fig 3, theory predicts that rotationally excited states, principally, $N = 2$ states, can be important in shaping the overall line profiles. For a sample temperature of 1.2 μK, the corresponding energy $k_BT \sim 25$ kHz is much smaller than the centrifugal energy ($\sim$150 kHz) of the $N = 2$ rotational levels for $n \sim 30$. Indeed, the calculations reveal that the $N = 2$ rotational levels are excited mainly from the high-energy tail ($\simeq 2.5k_BT$) of the thermal distribution [Eq. (13)], whereas the contributions to the $N = 0$ rotational levels mainly originate from closer to the peak of the thermal distribution. The small, but nonzero, initial relative kinetic energy of the collision pair [$\hbar^2k^2/(2\mu)$ in Eq. (14)] leads to the differences seen in Fig. 4 between the rotational energy spacings predicted by the present model and using Eq. (1).

Theory also suggests that, on average, for the lower values of n studied here, the production rates for ^{86}Sr dimers should be significantly smaller than those for ^{84}Sr dimers due to the strong interaction between ^{86}Sr atom pairs, which is reflected in a large near-resonant s-wave scattering length, $a_s = 811a_0$ [23]. This results from a node in the atomic scattering wave function [Eq. (10)] near $R = a_s$, whereupon the overlap $F_{v,N,M_N}(k, N', M'_N)$ with product dimer states with $R_n \simeq a_s$ is reduced, leading to suppression of the $N = 0$ dimer formation. (No comparably strong interaction exists between ^{84}Sr atom pairs where $a_s = 124a_0$ [32].) Due to the presence of a long-range centrifugal barrier, however, scattering for the higher partial waves will be little affected by the short-range scattering potential and the production rates for rotationally excited ^{84}Sr and ^{86}Sr dimers are predicted to be approximately equal. Indeed, the present analysis suggests that it is the suppression of the $N = 0$ channel for ^{86}Sr that facilitates observation of the rotationally excited states. The location of the node is close to the internuclear separation for dimers with $n \sim 25$, and as n and the dimer internuclear separations increase, the overlap $F_{v,N,M_N}(k, N', M'_N)$ become less sensitive to its presence. However, the effects of the node are still evident even for values of $n \sim 30$.

Comparison between the theoretical and experimental results for $n = 29$ in Fig. 3 shows that the measured relative production rates for $N = 0$ and $N = 2$ states are similar to those predicted by theory. Theory, however, suggests that essentially no $N = 3$ states will be created, whereas the data reveal the definite presence of a small signal associated with their formation. Furthermore, while theory does predict the formation of a small number of $N = 1$ states, this number is substantially less than suggested by the observations. The current theoretical model relies on the separation of the relative motion from the center-of-mass motion. A small anharmonicity together with the anisotropy of the trap may couple these two degrees of freedom and create rotationally excited states. The measured production rate for $n = 30$ ^{86}Sr dimers is significantly less than that seen for the neighboring $n = 29$ and 31 states. This is not suggested by theory and

appears to result from a local anomalous suppression of the $N = 0$ channel. (No similar local reduction in dimer formation was observed for ^{84}Sr dimers.) The origin of this suppression remains an open question. Coupling to molecular states with much shorter internuclear separations, for example, via resonant tunneling might shorten the lifetime of the $N = 0$ molecular level and suppress the contribution from $N = 0$ rotational states.

We turn now to the effects of recoil during photoexcitation, which are accentuated by taking data with the excitation lasers copropagating. In this case the effective photon recoil $\kappa/2 = (|\vec{\kappa}_1| + |\vec{\kappa}_2|)/2 \sim 7.6 \times 10^{-4}$ a.u. is larger by about a factor 3 compared to the counterpropagating case, and the argument of the Bessel function in Eq. (12), $\kappa R_n/2$, exceeds unity for $n \gtrsim 27$. Consequently, angular momentum transfer by photon recoil is no longer small. For example, for $n = 30$, $j_{\lambda=0}(\kappa R_n/2) = 0.85$, and $j_{\lambda=1}(\kappa R_n/2) = 0.29$; that is, the amplitude for transferring one unit of angular momentum in the transition is about 30% of that preserving the angular momentum. As a result, theory predicts that $N = 1$ states will provide a significant contribution to the observed excitation profiles.

A comparison between measurements undertaken using co- and counterpropagating laser beams is presented in Fig. 5 for $n = 29$ and sample temperatures of 1.2 and 2.0 μK, together with the corresponding theoretical predictions. All sets of measurements with co- and counterpropagating beams were undertaken on the same day to ensure near-identical trap conditions, and the laser linewidth was somewhat broader than when recording the data in Fig. 3. The change in the laser propagation directions affects the Doppler broadening. Numerical calculations (not shown) show a broadening by 20 kHz for the counterpropagating beams and 50 kHz for the copropagating ones. This broadening mainly originates from the translational motion of the molecule and can be well approximated by increasing the linewidth Γ in Eq. (14) (or replacing the Lorentzian by a Voigt profile). However, the measured spectra with the copropagating beams show not only a broadening but also a profile which flattens considerably near its peak, indicating excitation of the $N = 1$ level, which lies close to the $N = 0$ feature. Such behavior agrees with the theoretical predictions that the increase in recoil momentum will lead to a substantial increase in the relative production of $N = 1$ (and 3) excited rotational states. Additionally, at $T = 2\,\mu$K the calculated spectrum for the $N = 0$ level shows a slightly longer tail on the low-energy side, indicating the energy shift caused by the initial kinetic energy [Eq. (14)].

When using copropagating beams, the atomic recoil velocity, $\sim 2 \times 10^{-2}$ m s^{-1}, is somewhat larger than the typical thermal velocity of atoms in the trap, $\sim 1.4 \times 10^{-2}$ m s^{-1}. This suggests that, at least in part, the differences seen between the theoretically predicted and experimentally observed productions of the $N = 1$ and $N = 3$ levels when using counterpropagating laser beams might result because the atom sample has not reached thermal equilibrium and has a velocity distribution that contains a high-energy "tail" (losses from three-body recombination in the ^{86}Sr limit both the trap density and cooling effectiveness). Simulations indicate that the presence of such a tail could have a significant effect on the production of rotationally excited states. However, exhaustive measurements of the velocity distribution of atoms in the trap failed to reveal the presence of any significant high-energy tail, and the origin of the discrepancy remains in question. Nonetheless, it is clear that recoil can play an important role in determining the distribution of rotational states created.

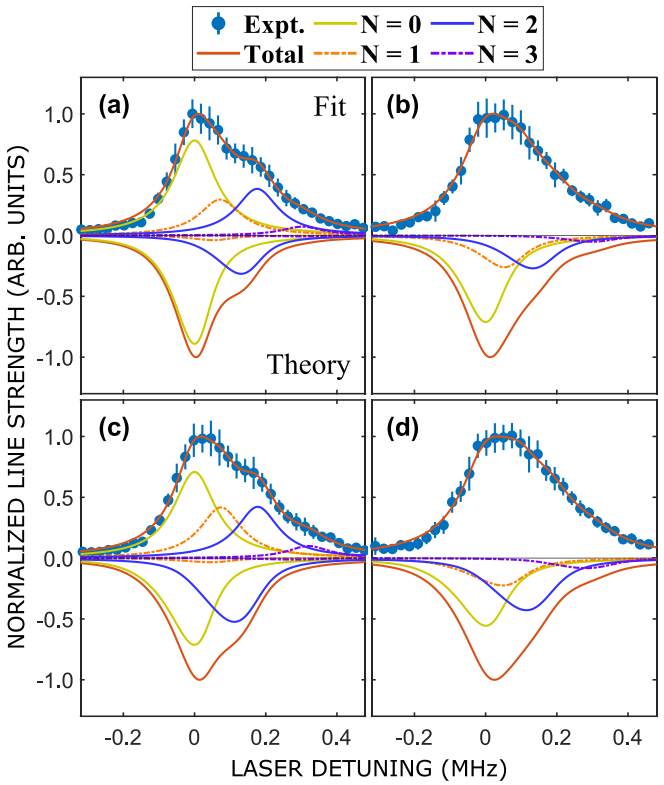

FIG. 5. Excitation spectra recorded for $n = 29$ ^{86}Sr dimers and sample temperatures of (a) and (b) 1.2 and (c) and (d) 2.0 μK using (a) and (c) counterpropagating laser beams and (b) and (d) copropagating laser beams. The corresponding theoretical predictions are also included. (a) and (c) include four component fits to the experimental data and their breakdowns. The lines through the experimental data in (b) and (d) are drawn as a guide to the eye. Breakdowns of the theoretical profiles into the contributions from each N level are also shown. To aid in their comparison, each data set is normalized to the same peak height.

IV. CONCLUSIONS

The present work showed that the large ^{86}Sr-^{86}Sr s-wave scattering length plays an important role when exciting ^{86}Sr dimers in a cold gas. In particular, it suppresses the formation of molecules in the ground rotational state, allowing rotationally excited states to be identified and measured spectroscopically. The data also highlight the important role played by momentum transfer during photoexcitation in enabling creation of $N = 1$ and 3 states. A simple theoretical model accounts for many of the observed features, but significant differences remain and suggest that more complex phenomena are at work than are captured by the present model. This promises fertile ground for future research which will be important for the use of Rydberg molecules as a probe of quantum gases [26].

ACKNOWLEDGMENTS

Research was supported by the AFOSR under Grant No. FA9550-17-1-0366, the NSF under Grant No. 1904294, and the FWF (Austria) under Grant No. FWF-SFB041 ViCom and the FWF Doctoral College W1243.

[1] C. H. Greene, A. S. Dickinson, and H. R. Sadeghpour, Creation of Polar and Nonpolar Ultra-Long-Range Rydberg Molecules, Phys. Rev. Lett. **85**, 2458 (2000).

[2] V. Bendkowsky, B. Butscher, J. Nipper, J. Shaffer, R. Low, and T. Pfau, Observation of ultralong-range Rydberg molecules, Nature (London) **458**, 1005 (2009).

[3] W. Li, T. Pohl, J. M. Rost, S. T. Rittenhouse, H. R. Sadeghpour, J. Nipper, B. Butscher, J. B. Balewski, V. Bendkowsky, R. Löw, and T. Pfau, A homonuclear molecule with a permanent electric dipole moment, Science **334**, 1110 (2011).

[4] J. Tallant, S. T. Rittenhouse, D. Booth, H. R. Sadeghpour, and J. P. Shaffer, Observation of Blueshifted Ultralong-Range Cs_2 Rydberg Molecules, Phys. Rev. Lett. **109**, 173202 (2012).

[5] B. J. DeSalvo, J. A. Aman, F. B. Dunning, T. C. Killian, H. R. Sadeghpour, S. Yoshida, and J. Burgdörfer, Ultra-long-range Rydberg molecules in a divalent atomic system, Phys. Rev. A **92**, 031403(R) (2015).

[6] M. A. Bellos, R. Carollo, J. Banerjee, E. E. Eyler, P. L. Gould, and W. C. Stwalley, Excitation of Weakly Bound Molecules to Trilobitelike Rydberg States, Phys. Rev. Lett. **111**, 053001 (2013).

[7] H. Saßmannshausen, F. Merkt, and J. Deiglmayr, Experimental Characterization of Singlet Scattering Channels in Long-Range Rydberg Molecules, Phys. Rev. Lett. **114**, 133201 (2015).

[8] A. T. Krupp, A. Gaj, J. B. Balewski, P. Ilzhöfer, S. Hofferberth, R. Löw, T. Pfau, M. Kurz, and P. Schmelcher, Alignment of *d*-State Rydberg Molecules, Phys. Rev. Lett. **112**, 143008 (2014).

[9] D. A. Anderson, S. A. Miller, and G. Raithel, Photoassociation of Long-Range *nd* Rydberg Molecules, Phys. Rev. Lett. **112**, 163201 (2014).

[10] D. Booth, S. T. Rittenhouse, J. Yang, H. R. Sadeghpour, and J. P. Shaffer, Production of trilobite Rydberg molecule dimers with kilo-debye permanent electric dipole moments, Science **348**, 99 (2015).

[11] M. T. Eiles and C. H. Greene, Ultracold Long-Range Rydberg Molecules with Complex Multichannel Spectra, Phys. Rev. Lett. **115**, 193201 (2015).

[12] M. T. Eiles, H. Lee, J. Pérez-Ríos, and C. H. Greene, Anisotropic blockade using pendular long-range Rydberg molecules, Phys. Rev. A **95**, 052708 (2017).

[13] J. D. Whalen, S. K. Kanungo, Y. Lu, S. Yoshida, J. Burgdörfer, F. B. Dunning, and T. C. Killian, Heteronuclear Rydberg molecules, Phys. Rev. A **101**, 060701(R) (2020).

[14] J. Gaj, A. T. Krupp, J. B. Balewski, R. Low, S. Hofferberth, and T. Pfau, From molecular spectra to a density shift in dense Rydberg gases, Nat. Commun. **5**, 4546 (2014).

[15] F. B. Dunning, T. C. Killian, S. Yoshida, and J. Burgdörfer, Recent advances in Rydberg physics using alkaline-earth atoms, J. Phys. B **49**, 112003 (2016).

[16] J. D. Whalen, F. Camargo, R. Ding, T. C. Killian, F. B. Dunning, J. Pérez-Ríos, S. Yoshida, and J. Burgdörfer, Lifetimes of ultralong-range strontium Rydberg molecules in a dense Bose-Einstein condensate, Phys. Rev. A **96**, 042702 (2017).

[17] F. Camargo, R. Schmidt, J. D. Whalen, R. Ding, G. Woehl, S. Yoshida, J. Burgdörfer, F. B. Dunning, H. R. Sadeghpour, E. Demler, and T. C. Killian, Creation of Rydberg Polarons in a Bose Gas, Phys. Rev. Lett. **120**, 083401 (2018).

[18] V. Bendkowsky, B. Butscher, J. Nipper, J. B. Balewski, J. P. Shaffer, R. Löw, T. Pfau, W. Li, J. Stanojevic, T. Pohl, and J. M. Rost, Rydberg Trimers and Excited Dimers Bound by Internal Quantum Reflection, Phys. Rev. Lett. **105**, 163201 (2010).

[19] R. Ding, S. K. Kanungo, J. D. Whalen, T. C. Killian, F. B. Dunning, S. Yoshida, and J. Burgdörfer, Creation of vibrationally-excited ultralong-range Rydberg molecules in polarized and unpolarized cold gases of ^{87}Sr, J. Phys. B **53**, 014002 (2020).

[20] B. H. Pate, Taking the pulse of molecular rotational spectroscopy, Science **333**, 947 (2011).

[21] J. Sous, H. R. Sadeghpour, T. C. Killian, E. Demler, and R. Schmidt, Rydberg impurity in a fermi gas: Quantum statistics and rotational blockade, Phys. Rev. Research **2**, 023021 (2020).

[22] K. M. Jones, E. Tiesinga, P. D. Lett, and P. S. Julienne, Ultracold photoassociation spectroscopy: Long-range molecules and atomic scattering, Rev. Mod. Phys. **78**, 483 (2006).

[23] J. A. Aman, J. C. Hill, R. Ding, K. R. A. Hazzard, T. C. Killian, and W. Y. Kon, Photoassociative spectroscopy of a halo molecule in ^{86}Sr, Phys. Rev. A **98**, 053441 (2018).

[24] T. Niederprüm, O. Thomas, T. Eichert, C. Lippe, J. Perez-Rios, C. H. Greene, and H. Ott, Observation of pendular butterfly Rydberg molecules, Nat. Commun. **7**, 12820 (2016).

[25] O. Thomas, C. Lippe, T. Eichert, and H. Ott, Photoassociation of rotating ultra-long range Rydberg molecules, J. Phys. B **51**, 155201 (2018).

[26] J. D. Whalen, S. K. Kanungo, R. Ding, M. Wagner, R. Schmidt, H. R. Sadeghpour, S. Yoshida, J. Burgdörfer, F. B. Dunning, and T. C. Killian, Probing nonlocal spatial correlations in quantum gases with ultra-long-range Rydberg molecules, Phys. Rev. A **100**, 011402(R) (2019).

[27] T. Schmid, C. Veit, N. Zuber, R. Löw, T. Pfau, M. Tarana, and M. Tomza, Rydberg Molecules for Ion-Atom Scattering in the Ultracold Regime, Phys. Rev. Lett. **120**, 153401 (2018).

[28] S. Stellmer, F. Schreck, and T. Killian, *Annual Review of Cold Atoms and Molecules* (World Scientific, Singapore, 2014)

[29] Y. N. MartinezdeEscobar, P. G. Mickelson, M. Yan, B. J. DeSalvo, S. B. Nagel, and T. C. Killian, Bose-Einstein Condensation of ^{84}Sr, Phys. Rev. Lett. **103**, 200402 (2009).

[30] J. A. Aman, Two-photon photoassociative spectroscopy of strontium-86, Ph.D. thesis, Rice University, 2019.

[31] J. D. Whalen, Probing nonlocal correlations with ultralong-range Rydberg molecules, Ph.D. thesis, Rice University, 2021.

[32] J.-C. Zhang, Z.-L. Zhu, Y.-F. Liu, and J.-F. Sun, Elastic scattering properties of ultracold strontium atoms, Chin. Phys. Lett. **28**, 123401 (2011).